



Magnetism and metallicity in moiré transition metal dichalcogenides

Patrick Tscheppe^{a,b}, Jiawei Zang^c, Marcel Klett^a, Seher Karakuzu^d, Armelle Celarier^e, Zhengqian Cheng^f, Chris A. Marianetti^f, Thomas A. Maier^g, Michel Ferrero^{e,h}, Andrew J. Millis^{c,d,1}, and Thomas Schäfer^{a,1}

Contributed by Andrew J. Millis; received July 6, 2023; accepted December 3, 2023; reviewed by Gregory S. Boebinger and Thierry Giamarchi

The ability to control the properties of twisted bilayer transition metal dichalcogenides *in situ* makes them an ideal platform for investigating the interplay of strong correlations and geometric frustration. Of particular interest are the low energy scales, which make it possible to experimentally access both temperature and magnetic fields that are of the order of the bandwidth or the correlation scale. In this manuscript, we analyze the moiré Hubbard model, believed to describe the low energy physics of an important subclass of the twisted bilayer compounds. We establish its magnetic and the metal–insulator phase diagram for the full range of magnetic fields up to the fully spin-polarized state. We find a rich phase diagram including fully and partially polarized insulating and metallic phases of which we determine the interplay of magnetic order, Zeeman-field, and metallicity, and make connection to recent experiments.

strongly correlated systems | moiré materials | magnetism | metal–insulator transitions

The correlation-driven Mott metal–insulator transition—in other words, under what circumstances can electrons move through a material—is one of the central issues in modern-day condensed matter physics. Developments over the past 5 y in moiré transition metal dichalcogenides, including the observation of a continuous Mott transition (1) and quantum criticality (2), have opened a new experimental frontier in this area (3–6). Moiré materials consist of two or more atomically thin layers, slightly mismatched by a combination of different lattice constants and stacking at small twist angles. The lattice mismatch and twist angle, combined with a weak but nonzero interlayer tunneling, produce experimental platforms whose low energy physics is described by a few-band model with a very large unit cell and therefore very low bandwidth and interaction scales, which moreover are tunable by twist angle, pressure, and the choice of materials in which the moiré system is embedded (3, 5). One particularly widely studied class of moiré materials are bilayers composed of transition metal dichalcogenide materials such as WSe₂ and MoTe₂ which in appropriate circumstances realize the moiré Hubbard model: A two-dimensional triangular lattice hosting a single band of electrons correlated by an interaction that to a good approximation may be taken to be site-local. Importantly, the magnitude and form of the interaction and the electronic band structure can be varied over wide ranges *in situ* by changing gate potentials and twist angles (4–8) while all electronic scales are small enough that temperatures and magnetic fields spanning the whole range from very low to higher than the effective bandwidth are experimentally accessible.

While the metal–insulator transition in two dimensional Hubbard models has been studied, both in general (9–16) and in connection to moiré systems (17, 18), the effect of a magnetic field seems apart from one notable exception (19) not to have been investigated, perhaps in part because for most conventional materials, the experimentally accessible fields are a tiny fraction of the bandwidth so that linear response theory suffices. Motivated by the wide range of field strengths experimentally accessible in moiré systems, in this paper, we use state-of-the-art single-site and cluster dynamical mean-field methods to study the metal–insulator phase diagram of the moiré Hubbard model over the full magnetic field range, assuming that the primary coupling is the Zeeman coupling to the electronic spin. Orbital effects (20–23) will be considered in a forthcoming paper. We reveal full and partially polarized insulating and metallic phases as well as canted antiferromagnetically ordered phases.

Model

Single layers of WSe₂ form a triangular lattice with strong spin–orbit coupling and inversion symmetry breaking. Stacking the layers at an appropriate small twist angle produces again a triangular lattice with a corresponding moiré lattice. At the twist

Significance

Putting two layers of transition metal dichalcogenides on top of each other and twisting them by a relative angle can create a multitude of fascinating physical phenomena like metal–insulator transitions and magnetism, that can be controlled to high accuracy. In this paper, we analyze the moiré Hubbard model, believed to capture the essential physics of such devices, by means of cutting-edge numerical methods. We establish the model's phase diagram as a function of temperature and applied magnetic fields. Apart from insulating magnetic phases, we also find metallic states at finite temperatures. Our findings represent an essential step toward the understanding of recent experiments and the model's applicability.

Author contributions: P.T., A.C., Z.C., C.A.M., T.A.M., M.F., A.J.M., and T.S. designed research; P.T., J.Z., M.K., S.K., A.C., Z.C., C.A.M., T.A.M., M.F., A.J.M., and T.S. performed research; P.T., J.Z., M.K., S.K., A.C., Z.C., C.A.M., T.A.M., M.F., A.J.M., and T.S. analyzed data; and P.T., M.K., A.J.M., and T.S. wrote the paper.

Reviewers: G.S.B., Florida State University; and T.G., Université de Genève.

The authors declare no competing interest.

Copyright © 2024 the Author(s). Published by PNAS. This article is distributed under [Creative Commons Attribution-NonCommercial-NoDerivatives License 4.0 \(CC BY-NC-ND\)](#).

¹To whom correspondence may be addressed. Email: amillis@flatironinstitute.org or t.schaefer@fkf.mpg.de.

This article contains supporting information online at <https://www.pnas.org/lookup/suppl/doi:10.1073/pnas.2311486121/-/DCSupplemental>.

Published January 11, 2024.

angles of relevance for recent experiments (1, 2), the relevant electronic states on the two layers are hybridized, leading to physics determined by a single spin-up band and a single spin-down band, and with different \mathbf{k} and spin states composed of different linear combinations of the individual layer states; this implies a spin-dependent hopping amplitude in the tight-binding model describing the moiré lattice (2, 24).

Motivated by these general considerations, as a low energy model, we study a modification of the well-known Hubbard model (25–28), a fundamental and widely studied model capturing the essential features of electronic correlations (29, 30): the so-called moiré Hubbard model (MHM) (24).

The Hamiltonian is

$$H = - \sum_{\langle ij \rangle, \sigma=\uparrow\downarrow} c_{i,\sigma}^\dagger t_{ij}^\sigma c_{j,\sigma} + U \sum_i n_{i,\uparrow} n_{i,\downarrow} - g \mu_B B \sum_{i,\alpha,\beta} c_{i,\alpha}^\dagger \sigma_z^{\alpha,\beta} c_{i,\beta}. \quad [1]$$

Here, i, j represent nearest-neighbor sites on a two-dimensional triangular lattice, U is the (purely local) Coulomb interaction, and $t_{ij}^\sigma = |t| e^{i\sigma\phi_{ij}}$ is a spin-dependent hopping parameter (24), which can be parameterized by a complex phase ϕ arising from the strong spin–orbit coupling of the constituent layers and a magnitude t . g is the gyromagnetic factor of an electron, μ_B is the Bohr magneton, and B an externally applied field in the z -direction. The structure of the model is such that at $\phi = \pi/6$ at half-filling the model has a particle–hole symmetry, a nested Fermi surface, and a third-order van Hove point, implying that at $T = B = 0$, the system is a 120° -antiferromagnetic insulator at even infinitesimal coupling; while for $\phi \neq \pi/6$, the model at $T = 0$ is a paramagnetic metal at small interaction strengths, with a first-order magnetic and metal–insulator transition as the relative interaction U/t is increased above a critical value, see ref. 24, and *SI Appendix*. Both t and ϕ may be experimentally tuned in situ by the application of appropriate gate voltages. In this work, we analyze the half-filled situation $\langle n_\uparrow \rangle + \langle n_\downarrow \rangle = 1$, considering both paramagnetic and 120° magnetically ordered states.

Zero Field Phase Diagram. For orientation and to demonstrate the robustness of our methods, we present in Fig. 1 the zero-field phase diagram of the fully nested ($\phi = \pi/6$) model in the temperature (T)-interaction (U) plane obtained from single-site and cluster dynamical mean-field methods. Paramagnetic insulator, paramagnetic metal, and antiferromagnetic insulator phases are found. The phase boundaries determined by the different methods are quantitatively similar almost everywhere, strongly suggesting that the results we find are insensitive to cluster effects. The only important difference is that, as is well known, the single-site DMFT method strongly overestimates the low T critical U needed to drive a paramagnetic metal–paramagnetic insulator phase transition; but it is important to note that the region of large difference occurs within the 120° -antiferromagnetic phase (i.e., below T_N) where the paramagnetic phase single-site DMFT calculation is irrelevant.

We remark that the calculations involve a mean-field approximation, so at finite N_c , the calculations do not capture the long-wavelength fluctuations that convert the transition to one of the Kosterlitz–Thouless type (for $\phi \neq 0$) or push the transition temperature to zero for the Heisenberg symmetry $\phi = 0$ case (32). The mean-field temperature found here should be interpreted as setting the scale at which magnetic fluctuations become both strong and long ranged.

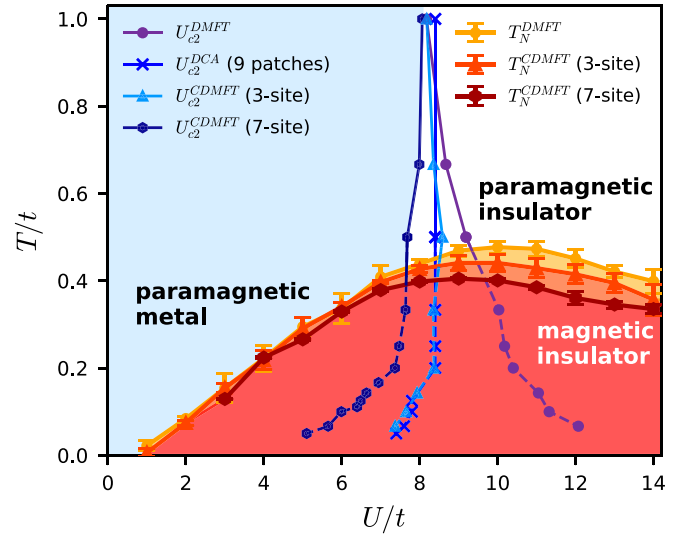


Fig. 1. Phase diagram of the moiré Hubbard model [Eq. 1] for $\phi = \pi/6$ at half-filling and zero external magnetic field $B = 0$ calculated by the dynamical mean-field methods indicated in the legends. Solid reddish lines denote magnetic phase transition lines from a paramagnetic to a 120° ordered antiferromagnetic state; solid blueish lines denote a cross-over from a metallic to an insulating region. Dashed blueish lines mark a metal–insulator cross-over when the calculation is restricted to a nonmagnetic (metastable) solution.

Applied Magnetic Field at $T = 0$. Turning now to the effects of a magnetic field, in Fig. 2A, we show the phase diagram in the magnetic field–interaction plane. This phase diagram was obtained at $T = 0$ using the single-site variational discrete action theory (VDAT), which has similar accuracy as the single-site DMFT, in the paramagnetic phase; however, spot checking the result with cluster methods and by allowing for magnetic order reveals that the single-site VDAT result for the full polarization line is quantitatively accurate. A fully spin-polarized, trivially insulating high-field phase is separated from a partially polarized phase by a transition line (sharp at $T = 0$). At small-to-intermediate interaction, the transition is continuous in the sense that the magnetization m_z in the paramagnetic phase evolves smoothly up to the saturation value $m_z = 1$, and our computed phase boundary agrees precisely with the Hartree–Fock result (24) and results from exact diagonalization (33). At larger interactions $U/t \gtrsim 6$, the transition changes to first order (meaning that m_z jumps from a value less than 1 to the saturated value) while the line deviates from the Hartree–Fock result and rolls over to the $\sim t^2/U$ saturation field expected for a Heisenberg magnet.

Also shown in the phase diagram is the paramagnetic (Mott) metal–insulator phase boundary. At the $\phi = \pi/6$ value used to construct Fig. 2, the metallic phase is reentrant: In the small range $12.5 \lesssim U/t \lesssim 14$, the zero B -field Mott insulator becomes metallic as the field is increased, before again becoming insulating. This reentrance is absent for $\phi = 0$ (see *SI Appendix* for the corresponding phase diagram), and it should be noted that cluster effects substantially change the single-site results for the Mott transition.

Applied Field at Nonzero Temperatures. We now incorporate magnetic ordering and nonzero temperatures in the analysis. We focus on the interaction strength $U/t = 4$, believed to be a suitable value for the description of the homobilayer WSe_2 (18). Fig. 2B–G show the Green functions and self-energies (minus

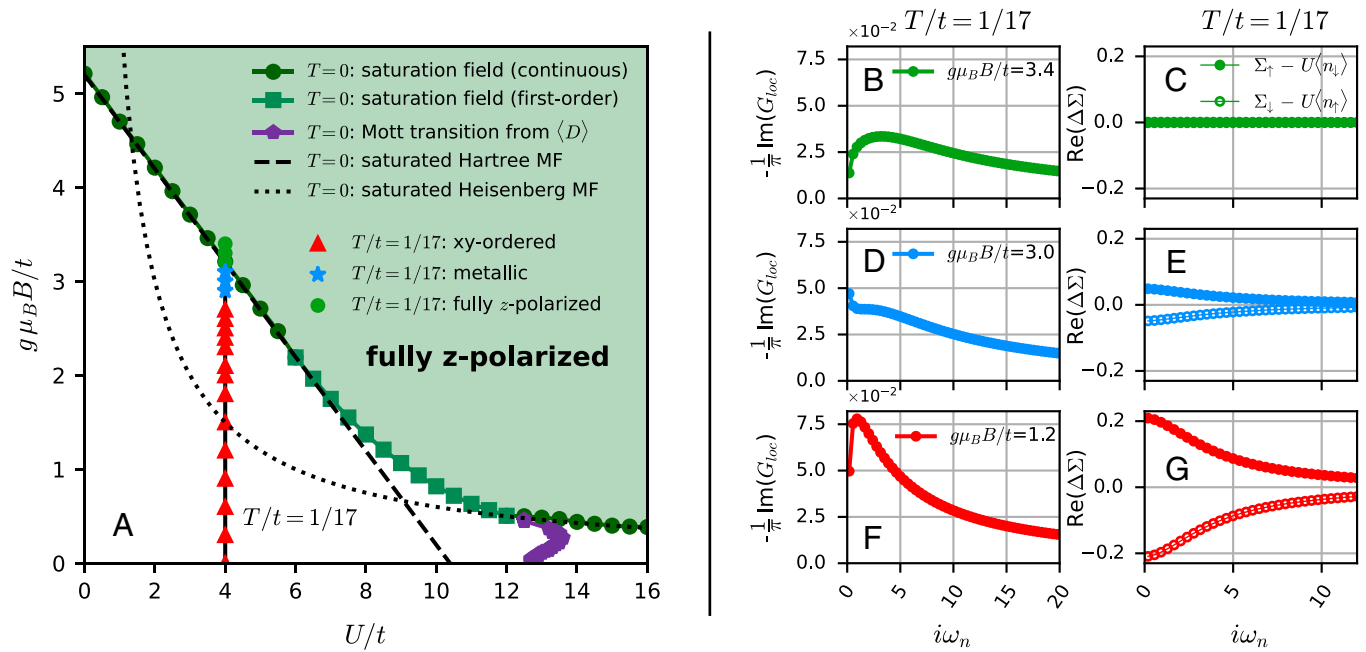


Fig. 2. (A) Zero temperature phase diagram for the half-filled perfectly nested MHM ($\phi = \pi/6$), calculated in the interaction strength (U)-magnetic field (B) plane at $T = 0$ using the VDAT method in the paramagnetic phase, i.e., without permitting spontaneous ordering. A phase boundary separates a large B , fully spin-polarized trivially insulating phase (green shaded region) from a small B partially spin-polarized phase. For $U/t \lesssim 6$ and $U/t \gtrsim 12$, the transition to the fully polarized phase is second order (green circles) while for $6 \lesssim U/t \lesssim 12$, the transition is first order (green squares). The dashed line shows the Hartree-Fock approximation to the full-polarization transition line. The dotted line shows the mean-field approximation to the full polarization transition of a nearest-neighbor Heisenberg model with $J \propto t^2/U$. Also shown is the critical coupling U_c of the Mott-Hubbard metal-insulator transition, which is seen to be reentrant as a function of field (purple pentagons). The vertical line at $U/t = 4$ indicates B fields at which a dynamical mean-field calculation at a temperature $T/t = 1/17 \approx 0.06$ leads to an antiferromagnetic insulator (red triangles), paramagnetic metal (blue stars), or trivial fully spin-polarized insulator (green circles). (B)–(G) Single-site dynamical mean-field results for the Matsubara frequency dependence of the imaginary part of the Green function (averaged over spin) and the two spin components of the dynamical self-energy $\Delta\Sigma = \Sigma(\omega) - \Sigma(\omega \rightarrow \infty)$ obtained at the nonzero temperature $T/t = 1/17$ for several magnetic fields along the vertical $U/t = 4$ line of (A).

their Hartree contributions) on the Matsubara axis, obtained from single-site DMFT at $T/t = 1/17$. At low field strengths $g\mu_B B/t = 1$, the system is insulating, indicated by the decrease in the imaginary part of the Green function at low Matsubara frequencies. This gap is opened by a strongly spin-dependent self-energy. At large field strengths $g\mu_B B/t \gtrsim 3.4$, the system is fully polarized, the lower $\sigma = \uparrow$ band is completely filled, and the combination of the magnetic field and the interaction opens a gap between the spin-up and spin-down bands. In between, e.g., at $g\mu_B B/t = 3$ and temperature $T/t = 1/17$, the xy -ordering is suppressed by the magnetic field; however, the system is not yet fully z -polarized, and, hence, the system is metallic.

We now turn to physical observables that can be obtained from these raw Green function data. Fig. 3A shows that as the Zeeman-field is increased from zero the staggered magnetization m_{xy} decreases and the uniform magnetization m_z increases, indicative of the spin canting expected for a Heisenberg-symmetry magnet and sketched on the figure. At the value $g\mu_B B/t = 2.8$, the staggered magnetization vanishes, but at this field, the uniform magnetization $m_z < 1$, indicating at this temperature, a small window of paramagnetic partially polarized phase separating the antiferromagnet from the fully polarized state.

Fig. 3B examines the evolution of the electronic properties of these states, plotting $\Xi := -dA/dT$, where $A = -\frac{1}{\pi T} G(\tau = \beta/2)$

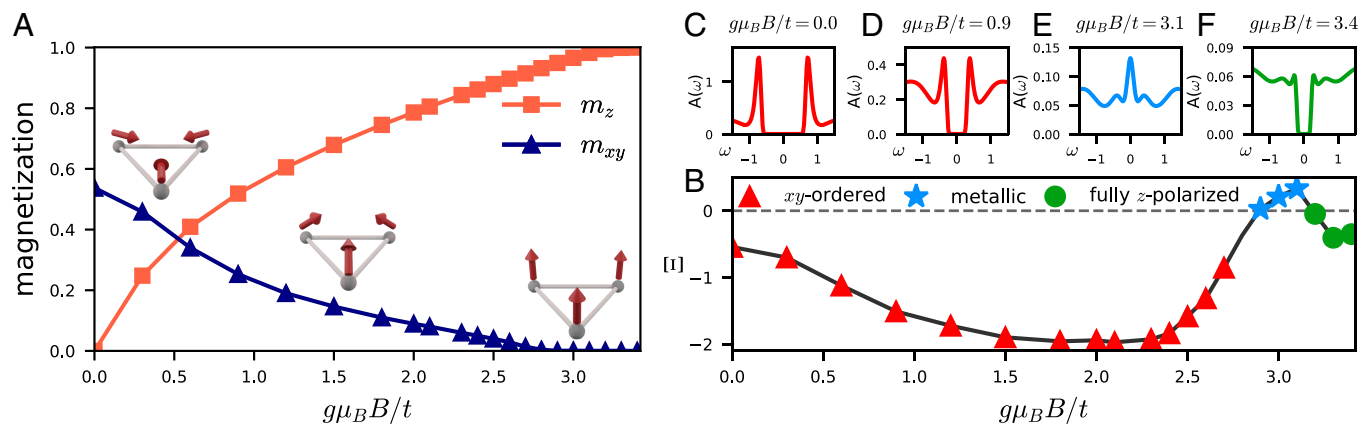


Fig. 3. (A) Magnetic field (B) dependence of antiferromagnetic order parameter m_{xy} (blue triangles) and spin polarization m_z (orange squares). (B) shows $\Xi = -dA/dT$ which is positive (negative) in metallic (insulating) phases (SI Appendix, Text). The local spectral functions (C)–(F), obtained with MaxEnt analytic continuation (34), confirm this classification. All quantities were computed at perfect nesting ($\phi = \pi/6$) for $U/t = 4$ and $T/t = 1/17$ with single-site DMFT.

is an estimate for the many-body density of states at the Fermi level. For the metallic state, $\Xi > 0$, whereas for the gapped states, $\Xi < 0$. The magnetic state at different fields is shown as colored symbols. Densities of states obtained by analytically continuing the Matsubara axis Green function are shown for several points in panels (C)–(F), confirming the identification of the different phases. We see that, at this value of U , insulating and magnetically ordered behavior are closely linked.

T-B Phase Diagrams and Generalizations. In order to demonstrate the robustness of our results, Fig. 4 presents the phase diagram in the field-temperature plane at $U/t = 4$ for a different phase angle ($\phi = \pi/8$), for which the nesting is imperfect and the van Hove singularity is removed from the Fermi surface. The analogous phase diagram for perfect nesting along with plots of the Fermi surface for the different values of ϕ can be found in *SI Appendix*. Although some quantitative features change compared to $\phi = \pi/6$ (for example, a smaller onset of the magnetic ordering temperature at zero B -field), the two phase diagrams are qualitatively very similar: Both show two types of magnetic ordering as well as an intermediate metallic phase.

The ordering temperature T_N (red triangles), denoting the second-order phase transition from a paramagnetic metal to a 120° ordered insulator, is reduced upon the application of the external field. Interestingly, as already pointed out before (and in contrast to $T = 0$), at nonzero temperatures, an intermediate metallic phase (blue stars) appears with partial z -polarization. At even larger fields, the system enters the fully polarized regime, which is insulating (green circles). At nonzero temperatures, the z -magnetization is never completely saturated; hence, we distinguish the partially polarized state from a “fully polarized” one using the criterion $m_z(B, T_{\text{pol}}) = 0.997$, which defines the boundary curve $T_{\text{pol}}(B)$ shown in Fig. 4.

We have found that, as the temperature is decreased, the range of B over which an intermediate metallic regime is observed decreases; the available evidence implies that at $T = 0$, the entire range from $B = 0$ up to the saturation field is xy -ordered and insulating, consistent with previous Hartree–Fock (24) and exact diagonalization results (33). Moreover, this remains the case even when the nesting (which favors the magnetic phase) is reduced. Finally, let us note that nonlocal (spatial) correlations, neglected by DMFT, do not change the picture drastically. This can be inferred from the comparison (and qualitative agreement) of DMFT with 9-site CDMFT calculations in Fig. 4B and is discussed further in *SI Appendix* (31).

Conclusions, Connection to Experiments, and Outlook. In this paper, we have investigated the full Zeeman magnetic field dependence of the metal–insulator and magnetic field phase diagram of the moiré Hubbard model (two-dimensional triangular lattice Hubbard model with xy -magnetic anisotropy and nontrivial hopping phase). Our focus on the Zeeman (spin) coupling and neglect of the orbital coupling is motivated by the large g -factor and still moderate lattice parameters available in current moiré systems (see ref. 24 for estimates to twist angles at which orbital effects will become relevant). Future work will address the orbital effects of the field. Our results substantially extend and generalize the important early work of Laloux and Georges on the infinite-dimensional Hubbard model (19). Our comparison of single-site and cluster dynamical mean-field approximations confirms that once magnetic ordering is allowed for, the single-site approximation provides a reasonably accurate solution even though the model is two-dimensional and that the VDAT method provides an extremely computationally efficient and highly accurate solution for ground-state properties. Within this approximation, we generally find, for both nested and nonnested cases, that at $T = 0$, the $B = 0$ magnetic order and insulating behavior persist over the entire $B > 0$ field range until the system becomes fully polarized, with the order parameter and transition temperature being gradually reduced by the spin canting. Metallic behavior is only found at nonzero temperatures for magnetic fields that suppress the magnetically ordered state to lower temperatures but are too weak to yield a fully spin-polarized state. Our results may be applicable to the recently studied twisted WSe₂ system. A precise comparison is difficult because the bandwidth cannot be unambiguously determined, but estimates from band theory (4) and quantum oscillation measurements on a sample with a moiré lattice constant of 6.3 nm suggest at low hole density a mass of $\approx 0.4 m_e$ implying $t \approx 2$ meV. Use of the band theory g -factor ≈ 6 and $U/t = 4$ would then suggest that a fully polarized state would occur at about 30 T. On the theoretical side, it would be of interest to investigate a multi-orbital or nonlocal interaction extension of the MHM analogously to an extended Hubbard model, see, e.g., refs. 35–37 as well as the role of superconductivity (38–40).

Materials and Methods

We investigate this model by means of the dynamical mean-field theory [DMFT (9, 41, 42)] in its single site and cluster forms. We employ two flavors of cluster DMFT: the cellular DMFT [CDMFT (43)] with center-focused post-processing (15)]

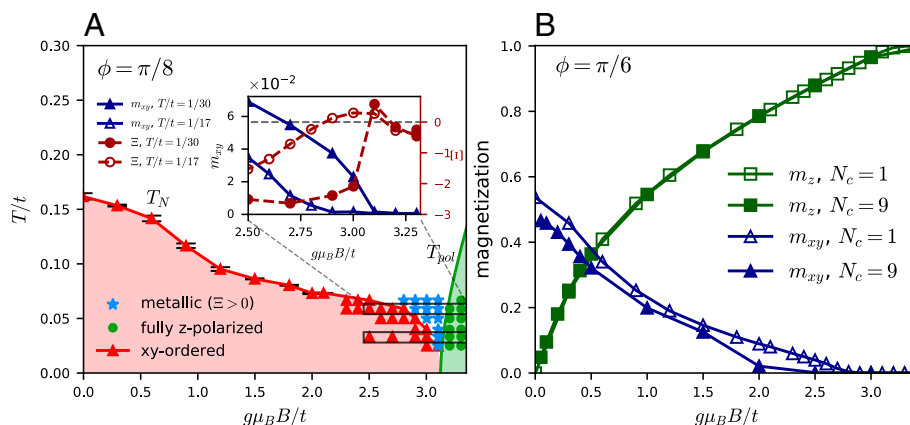


Fig. 4. (A) Phase diagram in the plane of temperature and Zeeman magnetic field, indicating magnetic and metallic phases computed for fixed $U/t = 4$ and $\phi = \pi/8$ (imperfect nesting), calculated by DMFT. (B) Comparison of DMFT and 9-site CDMFT for $T/t = 1/17$ and $\phi = \pi/6$ (perfect nesting).

and the dynamical cluster approximation [DCA (43)]. We use cluster sizes $N_c \in \{1, 3, 7, 9\}$. For our calculations at nonzero temperatures, we use continuous-time quantum Monte Carlo in its interaction expansion (CT-INT), using the TRIQS package (44), to solve the dynamical mean-field equations (45, 46). These methods provide results only above a certain low-temperature limit, which is typically low enough that a reliable extrapolation to the $T = 0$ physics is possible. For some of our calculations, we employ the recently developed VDAT (47–49) which provides an extremely computationally efficient estimate of ground-state properties of the single-site model. Details of the solvers, cluster geometries, and implementations are given in *SI Appendix*.

Data, Materials, and Software Availability. Data used to create Figures 1, 2, 3, 4 of the main text and S1, S13, and S5 are publicly available at https://github.com/patricktscheppe/magnetism_and-metallicity (50); Data for figures s2-s4 and S6–12 are included in the article and/or *SI Appendix*.

ACKNOWLEDGMENTS. We are grateful for fruitful discussions with Sabine Andergassen, Laura Classen, Lorenzo Del Re, Antoine Georges, Augusto Ghyotto, Lei Wang, Henri Menke, Abhay Pasupathy, Cory Dean, Michael Scherer, and Nils Wentzell. T.S., M.K., and M.F. acknowledge the hospitality of the Center for Computational Quantum Physics at the Flatiron Institute. We acknowledge the computer support teams at CPHT École Polytechnique and at the Flatiron Institute. We thank the computing service facility of the Max Planck Institute für Festkörperforschung (MPI-FKF) for their support. We gratefully

acknowledge use of the computational resources provided by the Max Planck Computing and Data Facility and by the IDCS mesocenter hosted at École Polytechnique. J.Z. acknowledges support from the NSF Materials REsearch Science and Engineering Center (MRSEC) program through the Center for Precision-Assembled Quantum Materials NSF-DMR-2011738 and A.J.M. was supported by Programmable Quantum Materials, an Energy Frontier Research Center funded by the U.S. Department of Energy (DOE), Office of Science, Basic Energy Sciences, under award DE-SC0019443. The work by T.A.M. was supported by the U.S. Department of Energy, Office of Science, Basic Energy Sciences, Materials Sciences and Engineering Division. An award of computer time was provided by the INCITE program. This research also used resources of the Oak Ridge Leadership Computing Facility, which is a DOE Office of Science User Facility supported under Contract DE-AC05-00OR22725. The work by Z.C. and C.A.M. was supported by the Columbia Center for Computational Electrochemistry. The Flatiron Institute is a division of the Simons Foundation.

Author affiliations: ^aIndependent Research Group, Max-Planck-Institut für Festkörperforschung, Stuttgart 70569, Germany; ^bInstitut für Theoretische Physik and Center for Quantum Science, Universität Tübingen, Tübingen 72076, Germany; ^cDepartment of Physics, Columbia University, New York, NY 10027; ^dCenter for Computational Quantum Physics, Flatiron Institute, New York, NY 10010; ^eCPHT, CNRS, École Polytechnique, Institut Polytechnique de Paris, Palaiseau 91128, France; ^fDepartment of Applied Physics and Applied Mathematics, Columbia University, New York, NY 10027; ^gComputational Sciences and Engineering Division, Oak Ridge National Laboratory, Oak Ridge, TN 37831-6164; and ^hCollège de France, Paris 75005, France

1. T. Li *et al.*, Continuous Mott transition in semiconductor moiré superlattices. *Nature* **597**, 350–354 (2021).
2. A. Ghyotto *et al.*, Quantum criticality in twisted transition metal dichalcogenides. *Nature* **597**, 345–349 (2021).
3. Y. Tang *et al.*, Simulation of Hubbard model physics in WSe₂/WS₂ moiré superlattices. *Nature* **579**, 353–358 (2020).
4. L. Wang *et al.*, Correlated electronic phases in twisted bilayer transition metal dichalcogenides. *Nat. Mater.* **19**, 861–866 (2020).
5. D. M. Kennes *et al.*, Moiré heterostructures as a condensed-matter quantum simulator. *Nat. Phys.* **17**, 155–163 (2021).
6. F. Wu, T. Lovorn, E. Tutuc, A. H. MacDonald, Hubbard model physics in transition metal dichalcogenide moiré bands. *Phys. Rev. Lett.* **121**, 026402 (2018).
7. F. Wu, T. Lovorn, E. Tutuc, I. Martin, A. H. MacDonald, Topological insulators in twisted transition metal dichalcogenide homobilayers. *Phys. Rev. Lett.* **122**, 086402 (2019).
8. H. Pan, F. Wu, S. Das Sarma, Band topology, Hubbard model, Heisenberg model, and Dzyaloshinskii-Moriya interaction in twisted bilayer WSe₂. *Phys. Rev. Res.* **2**, 033087 (2020).
9. A. Georges, G. Kotliar, M. Krauth, M. J. Rozenberg, Dynamical mean-field theory of strongly correlated fermion systems and the limit of infinite dimensions. *Rev. Mod. Phys.* **68**, 13 (1996).
10. O. Parcollet, G. Biroli, G. Kotliar, Cluster dynamical mean field analysis of the Mott transition. *Phys. Rev. Lett.* **92**, 226402 (2004).
11. S. Moukouri, M. Jarrell, Absence of a Slater transition in the two-dimensional Hubbard model. *Phys. Rev. Lett.* **87**, 167010 (2001).
12. T. Schäfer *et al.*, Fate of the false Mott-Hubbard transition in two dimensions. *Phys. Rev. B* **91**, 125109 (2015).
13. T. Schäfer, A. Toschi, K. Held, Dynamical vertex approximation for the two-dimensional Hubbard model. *J. Magnet. Magnet. Mater.* **400**, 107–111 (2016). Proceedings of the 20th International Conference on Magnetism (Barcelona) 5–10 July 2015.
14. A. Wietek *et al.*, Mott insulating states with competing orders in the triangular lattice Hubbard model. *Phys. Rev. X* **11**, 041013 (2021).
15. M. Klett *et al.*, Real-space cluster dynamical mean-field theory: Center-focused extrapolation on the one- and two-particle levels. *Phys. Rev. Res.* **2**, 033476 (2020).
16. P. O. Downey, O. Gingras, M. Charlebois, C. D. Hébert, A. M. S. Tremblay, Mott transition, Widom line, Frenkel line and pseudogap in the half-filled triangular lattice Hubbard model (2022).
17. N. Morales-Durán, A. H. MacDonald, P. Potasz, Metal-insulator transition in transition metal dichalcogenide heterobilayer moiré superlattices. *Phys. Rev. B* **103**, L241110 (2021).
18. J. Zang, J. Wang, J. Cano, A. Georges, A. J. Millis, Dynamical mean-field theory of moiré bilayer transition metal dichalcogenides: Phase diagram, resistivity, and quantum criticality. *Phys. Rev. X* **12**, 021064 (2022).
19. L. Laloux, A. Georges, W. Krauth, Effect of a magnetic field on Mott-Hubbard systems. *Phys. Rev. B* **50**, 3092–3102 (1994).
20. S. Acheche, L. F. Arsenault, A. M. S. Tremblay, Orbital effect of the magnetic field in dynamical mean-field theory. *Phys. Rev. B* **96**, 235135 (2017).
21. A. A. Markov, G. Rohringer, A. N. Rubtsov, Robustness of the topological quantization of the Hall conductivity for correlated lattice electrons at finite temperatures. *Phys. Rev. B* **100**, 115102 (2019).
22. J. Vučković, R. Žitko, Electrical conductivity in the Hubbard model: Orbital effects of magnetic field. *Phys. Rev. B* **104**, 205101 (2021).
23. J. Vučković, R. Žitko, Universal magnetic oscillations of DC conductivity in the incoherent regime of correlated systems. *Phys. Rev. Lett.* **127**, 196601 (2021).
24. J. Zang, J. Wang, J. Cano, A. J. Millis, Hartree-Fock study of the moiré Hubbard model for twisted bilayer transition metal dichalcogenides. *Phys. Rev. B* **104**, 075150 (2021).
25. J. Hubbard, Electron correlations in narrow energy bands. *Proc. R. Soc. London. Ser. A Math. Phys. Sci.* **276**, 238–257 (1963).
26. J. Hubbard, B. H. Flowers, Electron correlations in narrow energy bands III. An improved solution. *Proc. R. Soc. London Sect. A* **281**, 401–419 (1964).
27. M. C. Gutzwiller, Effect of correlation on the ferromagnetism of transition metals. *Phys. Rev. Lett.* **10**, 159–162 (1963).
28. J. Kanamori, Electron correlation and ferromagnetism of transition metals. *Prog. Theor. Phys.* **30**, 275–289 (1963).
29. M. Qin, T. Schäfer, S. Andergassen, P. Corboz, E. Gull, The Hubbard model: A computational perspective. *Annu. Rev. Condens. Matter Phys.* **13**, 275–302 (2022).
30. D. P. Arovas, E. Berg, S. A. Kivelson, S. Raghu, The Hubbard model. *Annu. Rev. Condens. Matter Phys.* **13**, 239–274 (2022).
31. N. D. Mermin, H. Wagner, Absence of ferromagnetism or antiferromagnetism in one- or two-dimensional isotropic Heisenberg models. *Phys. Rev. Lett.* **17**, 1307 (1966).
32. A. Wietek *et al.*, Tunable stripe order and weak superconductivity in the Moiré Hubbard model. *Phys. Rev. Res.* **4**, 043048 (2022).
33. G. J. Krabberger, R. Triebl, M. Zingl, M. Aichhorn, Maximum entropy formalism for the analytic continuation of matrix-valued Green's functions. *Phys. Rev. B* **96**, 155128 (2017).
34. N. Gneist, L. Classen, M. M. Scherer, Competing instabilities of the extended Hubbard model on the triangular lattice: Truncated-unity functional renormalization group and application to moiré materials. *Phys. Rev. B* **106**, 125141 (2022).
35. Y. Zhou, D. N. Sheng, E. A. Kim, Quantum phases of transition metal dichalcogenide moiré systems. *Phys. Rev. Lett.* **128**, 157602 (2022).
36. G. Mazza, A. Amaricci, Strongly correlated exciton-polarons in twisted homobilayer heterostructures. *Phys. Rev. B* **106**, L241104 (2022).
37. M. Bélanger, J. Fournier, D. Sénéchal, Superconductivity in the twisted bilayer transition metal dichalcogenide WSe₂: A quantum cluster study. *Phys. Rev. B* **106**, 235135 (2022).
38. L. Klebl, A. Fischer, L. Classen, M. M. Scherer, D. M. Kennes, Competition of density waves and superconductivity in twisted tungsten diselenide. *Phys. Rev. Res.* **5**, L012034 (2023).
39. Y. M. Wu, Z. Wu, H. Yao, Pair-density-wave and chiral superconductivity in twisted bilayer transition metal dichalcogenides. *Phys. Rev. Lett.* **130**, 126001 (2023).
40. W. Metzner, D. Vollhardt, Correlated lattice fermions in $d = \infty$ dimensions. *Phys. Rev. Lett.* **62**, 324–327 (1989).
41. A. Georges, G. Kotliar, Hubbard model in infinite dimensions. *Phys. Rev. B* **45**, 6479–6483 (1992).
42. T. Maier, M. Jarrell, T. Pruschke, M. H. Hettler, Quantum cluster theories. *Rev. Mod. Phys.* **77**, 1027–1080 (2005).
43. O. Parcollet *et al.*, Triqs: A toolbox for research on interacting quantum systems. *Comput. Phys. Commun.* **196**, 398–415 (2015).
44. A. N. Rubtsov, V. V. Savkin, A. I. Lichtenstein, Continuous-time quantum Monte Carlo method for fermions. *Phys. Rev. B* **72**, 035122 (2005).
45. E. Gull *et al.*, Continuous-time Monte Carlo methods for quantum impurity models. *Rev. Mod. Phys.* **83**, 349 (2011).
46. Z. Cheng, C. A. Marianetti, Variational discrete action theory. *Phys. Rev. Lett.* **126**, 206402 (2021).
47. Z. Cheng, C. A. Marianetti, Foundations of variational discrete action theory. *Phys. Rev. B* **103**, 195138 (2021).
48. Z. Cheng, C. A. Marianetti, Precise ground state of multiorbital Mott systems via the variational discrete action theory. *Phys. Rev. B* **106**, 205129 (2022).
49. Z. Cheng, C. A. Marianetti, Gauge constrained algorithm of variational discrete action theory at $N = 3$ for the multiorbital Hubbard model. *Phys. Rev. B* **108**, 035127 (2023).
50. P. Tschepp *et al.*, Data used to create figures 1, 2, 3, 4 and S1, S5, and S13. GitHub. https://github.com/patricktscheppe/magnetism_and-metallicity. Deposited 20 December 2023.